Subdiffraction-limited imaging based on longitudinal modes in a spatially dispersive slab

Avner Yanai and Uriel Levy[*]

Department of Applied Physics, The Benin School of Engineering and Computer Science, The Hebrew University of Jerusalem, Israel

It was proposed that a flat silver layer could be used to form a subdiffraction-limited image when illuminated near its surface plasmon resonance frequency [J. B. Pendry, Phys. Rev. Lett. **85**, 3966 (2000)]. In this paper, we study the possibility of obtaining sub diffraction resolution using a different mechanism, with no surface plasmons involved. Instead, by taking into account the nonlocal response of a thin silver slab, we show that longitudinal modes contribute to the formation of a subdiffraction-limited image in a frequency regime above the plasma frequency. The differences between these two distinct mechanisms are studied and explained.

I. INTRODUCTION

In 2000, it was suggested that a thin planar metallic slab can perform as a lens capable of producing an image with subdiffraction-limited (SDL) resolution [1]. In this seminal paper, Pendry showed that by using a thin metallic slab, only few tens of nanometers thick, which is excited with light near its surface plasmon (SP) resonance frequency, an image with SDL size can be obtained, due to the high momentum frequency components of the SP modes that are supported by the interfaces between the metallic slab and the dielectric medium surrounding it. This concept of a homogeneous slab performing as a lens was a variant (perhaps more realistic) based on previous work of Veselago that showed that ideal negative index slab behaves as a lens [2]. Pendry also claimed that the resolution of such an ideal negative index slab is not limited [1]. It is now common to coin the ideal negative index slab configuration as a "perfect lens," while a thin metallic layer is now defined as a "poor man's lens." Both types of lenses became the subject of debate and controversy [3]. The discussion was further stimulated by the experimental demonstration of the "poor man's lens," obtaining resolution of the order of $\sim\lambda_0/10$ (λ_0 being the vacuum wavelength) [4–6]. Part of the debate regarding the poor man's lens was concerned with the fact that a momentum cutoff of the SP modes is inherent, due to the nonlocal response of the metal permittivity function [7–10]. In the nonlocal description, the permittivity function is described by $\varepsilon(\omega,\mathbf{k})$; i.e., it is a function of both the optical frequency ω and the propagation constant $\mathbf{k}$, due to temporal and spatial dispersion, respectively. For small k vectors, one can neglect spatial dispersion and assume that $\varepsilon(\omega,\mathbf{k}) \approx \varepsilon(\omega)$. However, for large k vectors, the SP modes reach a momentum cutoff resulting in a fundamental resolution limit for perfect imaging. A detailed analysis, however, showed that the "poor man's lens" performance is very similar under both local and nonlocal approximations, because the ohmic losses inherent to the metal deteriorate the image even more drastically as compared with nonlocal effects [11]. Nonlocal effects for metallic slabs are pronounced when the slab thickness is less than the 10-nm regime. For these dimensions, it was shown that the absorption spectrum above the plasma frequency (ω_p) exhibits oscillations due to

Fabry-Perot (FP) resonances of longitudinal modes, which are modes with zero magnetic field, and electric field vector **E** parallel to the propagation vector **k**. Longitudinal modes satisfy the macroscopic Maxwell's equations when $\varepsilon(\omega,\mathbf{k}) = 0$ [12–14]. For several metals such as alkali metals and silver, a phenomenological description of $\varepsilon(\omega,\mathbf{k})$ can be obtained by employing the linearized hydrodynamic model [15–20]. This model successfully reproduces the appearance of longitudinal mode resonances, which were experimentally observed for thin layered metals [21], and offers a qualitative explanation for the blue shifting of the localized SP resonance observed in silver nanoparticles [22–25]. These results cannot be explained with local models. However, the validity of this model is challenged to account for quantum-sized effects [26–29]. In general, a full quantum-mechanical calculation is needed for an accurate account of the nonlocal response. However, the longitudinal mode resonance effect (described below) that is in the heart of this paper is fully accounted for by the hydrodynamic model. In this paper, we propose a different physical concept for achieving SDL imaging, taking advantage of the longitudinal modes within a thin metallic slab that is described by the hydrodynamic model. The SDL imaging occurs for discrete frequencies satisfying $\omega > \omega_p$. This frequency regime is different from the original proposal of the "poor man's lens," in which the incident illumination frequency is in the vicinity of the SP resonance frequency $\omega_p/\sqrt{2}$. Furthermore, the underlying physical mechanism of the two approaches is different. In the original proposal, the high-k components of the source are reconstructed in the image by the SP resonance surface modes, which support high spatial frequency components. In contrast, our approach is not based on surface modes. Instead, the high-k components are transferred to the image plane by the longitudinal modes, which typically have propagation constants more than an order of magnitude larger than the vacuum propagation constant $k_0 = 2\pi/\lambda_0$. The paper is structured as follows. In Sec. II we describe the modes inherent to the nonlocal slab-lens geometry. In Sec. III we present results based on this formalism. Sec. IV concludes the paper.

II. MODAL ANALYSIS

Our lens geometry consists of a slab infinitely extending along the x and y coordinates and bound between $z = 0$ and

---

[*]ulevy@mail.huji.ac.il
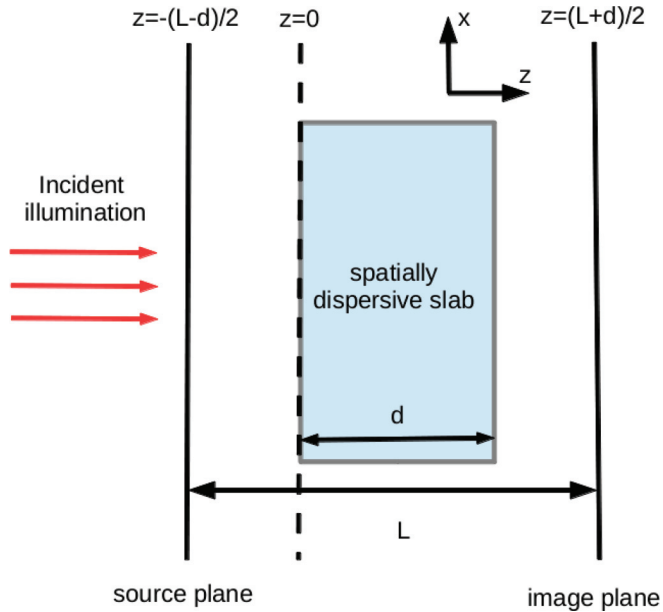
FIG. 1. (Color online) Schematics of a spatially dispersive slab of thickness d, surrounded by vacuum.

$z = d$ (see schematic in Fig. 1). The image and source planes are located at $z = -(L - d)/2$ and $z = (L + d)/2$, respectively. In our analysis we assume that the slab is surrounded by vacuum. We consider TM polarization illumination, i.e., $\mathbf{E} = E_x \hat{\mathbf{x}} + E_z \hat{\mathbf{z}}$, for which plasmonic and longitudinal modes exist. The permittivity of the slab is described by the hydrodynamic model. From this model it follows that for transverse modes ($\mathbf{E} \perp \mathbf{k}$) the permittivity function follows the well-known Drude model $\varepsilon_T(\omega) = 1 - \frac{\omega_p^2}{\omega^2 + i\gamma\omega}$, while for the longitudinal modes ($\mathbf{E} \parallel \mathbf{k}$) the material response is given by $\varepsilon_L(\omega, \mathbf{k}) = 1 - \frac{\omega_p^2}{\omega^2 + i\gamma\omega - \beta^2 k^2}$. Here, γ is the damping constant, and β defines the strength of the nonlocal response. The electric fields of the transverse modes are given by $\mathbf{E_T} = E_T(-k_{z,T}/k_x \hat{\mathbf{x}} + \hat{\mathbf{z}}) \exp[j(k_x x + k_{z,T} z)]$, and the propagation constant of the transverse mode satisfies the dispersion relation $k_{z,T}^2 = \varepsilon_T \omega^2/c^2 - k_x^2$. The electric fields of the longitudinal mode is given by $\mathbf{E_L} = E_L(k_x/k_{z,L} \hat{\mathbf{x}} + \hat{\mathbf{z}}) \exp[j(k_x x + k_{z,L} z)]$, and its propagation constant is given by $k_{z,L}^2 = [\omega(\omega + i\gamma) - \omega_p^2]/\beta^2 - k_x^2$, which follows directly from the longitudinal mode dispersion relation $\varepsilon_L(\omega, \mathbf{k}) = 0$. Because the spatially dispersive slab supports twice the number of modes a nonspatially dispersive slab does, an additional boundary condition (ABC) is needed other than the two conventional conditions of continuity of the transverse fields, in order to solve for all modal amplitudes [12,14,30,31]. For an air-metal interface the set of boundary conditions we assume are the continuity of E_x, E_z and the normal current J_z. Employing these boundary conditions and preserving the continuity of k_x, one obtains the expression for the complex transmission amplitude T [32]. For completeness, the derivation for the transmission amplitude is presented in the Appendix.

III. RESULTS AND INTERPRETATION

We now turn into studying the transmission through an Ag slab for the following parameters [33]: $\omega_p = 9.6$ eV, $\gamma = (1/420)\omega_p$, $\beta^2 = (3/5)/v_F^2$, and $v_F = 4.63 \times 10^{-3}c$. Here v_F and c are the Fermi velocity and the speed of light in vacuum, respectively. Possible surface roughness of the layer is not taken into account in our simplified model (see Ref. [16], Sec. 4D). We continue our study assuming this set of parameters, although the concepts derived below are general and support any spatially dispersive material, which can be described by the hydrodynamic model. In Fig. 2(a) we plot $\log(|T|^2)$ as a function of ω and k_x for the case of SP resonance, where the frequency ω is in the vicinity of $\omega_p/\sqrt{2}$, assuming layer thickness of $d = 3$ nm. Two SP resonances with k_x components below the light line are observed. From previous studies [3,34–36], it is known that it is the interplay between the two modes that allows for the reconstruction of an image with SDL resolution, due to the very high transmission coefficients of plane waves with large k_x (mind the logarithmic scale bar). In Fig. 2(b) we calculate $|T|^2$ assuming the same slab thickness; however, we now consider a different frequency interval ($\omega_p < \omega < 1.5\omega_p$). In this frequency range, $k_{z,L}$ becomes predominantly real. Moreover, for the assumed ultrathin slab dimensions, the longitudinal modes exhibit distinguishable FP resonances at discrete frequencies satisfying $k_{z,L} d/\pi = N$, where N is an odd number (Ref. [14], Sec. 3.2). A detailed view of one of these FP modes ($N = 11$) at $\sim 1.31\omega_p$ is shown in Fig. 2(c). At these resonance frequencies, the spectrum of $|T|^2$ shows transmission peaks, which are nearly uniform in frequency over a large range of k_x values. Therefore, the transmission spectrum at one of these resonant frequencies seems to be more appealing for reconstruction of an SDL image (which typically contains a large span of k_x values) as compared to the SP resonance case, which is more dispersive in nature, as shown in Fig. 2(a). On the other hand, the overall transmission magnitude of these longitudinal modes is lower as compared to the SP modes [note that Fig. 2(a) is in logarithmic scale while Fig. 2(b) is not!]. In addition to the FP transmission peaks, which are evident for large values of k_x, we also notice in Fig. 2(b) the existence of a region with nearly uniform transmission for low values of k_x, which are above the light cone. In this region the transmission is ~ 1, besides discrete dips in transmission corresponding to the FP modes. The FP modes exist mathematically for $\omega > \omega_p$, but since Im($k_{z,L}$) grows with ω, the resonance effect diminishes with the frequency. We next turn into a further comparison between the two approaches, with the goal of identifying the inherent properties and advantages of each approach.

To perfectly image a line source, one needs both the transmission magnitude and the transmission phase to be constant with k_x (Ref. [37], Sec. 2.2.1). In Fig. 2(d) we plot the normalized phase of transmission $\arg(T)/\pi$ as a function of k_x for several frequencies near $1.31\omega_p$, to estimate how uniform is the phase for different spatial frequencies. In Fig. 2(e) we plot the magnitude of the E_z in the slab for a specific FP resonance of the longitudinal modes ($\omega = 1.31\omega_p$ and $k_x = 6\omega_p/c$). In Fig. 2(f) we plot the dependence of the real and imaginary part of $k_{z,L}$, as a function of k_x, for $\omega = 1.31\omega_p$. It is seen that the variation in $k_{z,L}$ is negligible ($\sim 0.1\%$ in its real value
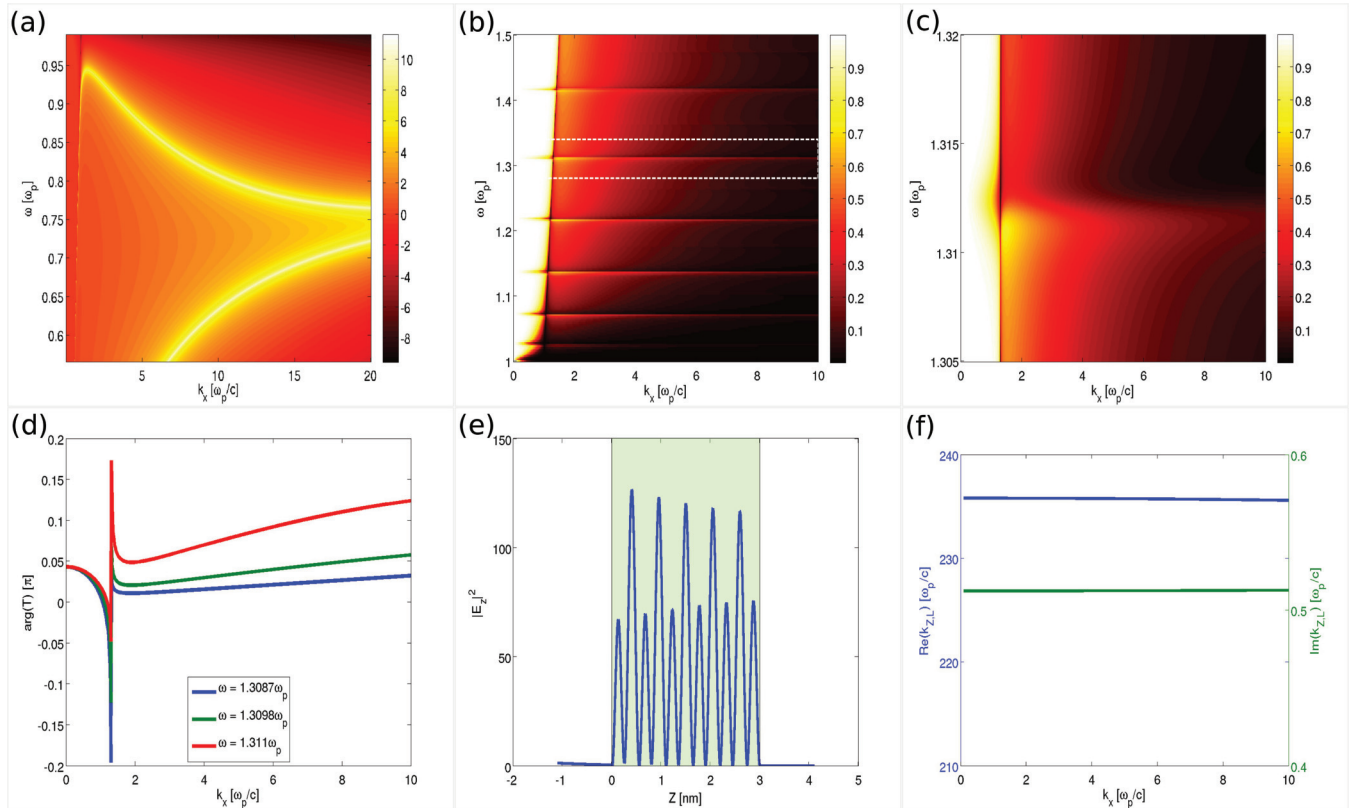
FIG. 2. (Color online) (a) $\log(|T|^2)$ as function of ω and k_x in the vicinity of $\omega_p/\sqrt{2}$ (plasmonic resonance regime) and $d = 3$ nm. (b) $|T|^2$ as function of ω and k_x for $\omega_p < \omega < 1.5\omega_p$ (longitudinal mode FP regime) and $d = 3$ nm. (c) Detailed view of the FP resonance with $N = 11$ near $\omega = 1.31\omega_p$. (d) The argument of the complex slab transmission coefficient T in units of π, calculated for several frequencies near the $N = 11$ FP resonance. (e) Distribution of $|E_z|^2$ in the slab (green background), calculated for $d = 3$ nm, $\omega = 1.31\omega_p$, and $k_x = 6\omega_p/c$. (f) Real (blue line) and imaginary (green line) parts of $k_{z,L}$ as function of k_x, calculated for $\omega = 1.31\omega_p$.

and $\sim 1\%$ in its imaginary value). This is primarily due to its large value, which is the key reason for the FP transmission resonances shown in Fig. 2(b) being nearly flat with k_x.

To estimate the imaging capabilities of the lens, we define two point spread functions (PSF), by calculating the transmission function at the image plane obtained by summation of an infinite number of plane waves according to:

$$\text{PSF}_{E_x}(x,\omega) = \int_0^\infty -(k_{z0}/k_x)T(k_x,\omega) \exp[j(L-d)k_{z0}$$
$$+ jk_x x]dk_x + \int_0^\infty -(k_{z0}/k_x)T(k_x,\omega)$$
$$\times \exp[j(L-d)k_{z0} - jk_x x]dk_x, \quad (1)$$

$$\text{PSF}_{E_z}(x,\omega) = \int_0^\infty T(k_x,\omega) \exp$$
$$\times [j(L-d)k_{z0} + jk_x x]dk_x - \int_0^\infty T(k_x,\omega)$$
$$\times \exp[j(L-d)k_{z0} - jk_x x]dk_x. \quad (2)$$

Here, PSF_{E_x} and PSF_{E_z} correspond to the PSF of the E_x and E_z electric field components, respectively. The vacuum propagation constant k_{z0} is defined by $k_{z0}^2 = \omega^2/c^2 - k_x^2$. Equations (1) and (2) are defined for the case of E_x polarized illumination. Following these definitions, we also define the

total PSF in the image plane as:

$$\text{PSF}_T = \left|\text{PSF}_{E_x}\right|^2 + \left|\text{PSF}_{E_z}\right|^2 \quad (3)$$

In Fig. 3 the normalized transmission magnitude $|\text{PSF}_T|^2/|\max(\text{PSF}_T)|^2$ in the image plane is plotted for several imaging distances $(L - d)$. The legend shows the normalization factor $|\max(\text{PSF}_T)|^2$ for each imaging distance. Figures 3(a) and 3(b) show the results obtained for the longitudinal mode FP resonance with $N = 11$ ($\omega = 1.31\omega_p$) and $N = 5$ ($\omega = 1.0681\omega_p$), respectively. Figure 3(c) is calculated for $\omega = 0.7071\omega_p$, corresponding to the plasmonic resonance. For the case where the source is positioned at the surface of the slab ($L - d = 0$, red line) the longitudinal mode FP mechanism results in an ultranarrow FWHM of less than 2 nm, for both FP resonances. However, when the imaging distance increases, the FWHM increases and substantial broadening of the PSF_T is observed. We note that the PSFs of the two FP resonances [Figs. 3(a) and 3(b)] are relatively similar. Once again, this is the outcome of the relatively flat dispersion curves of the FP modes. In contrast, the plasmonic resonance [Fig. 3(c)] behaves very differently. One may observe that the PSF_T is narrower when the source is slightly away of the surface ($L - d = 3$ and 6 nm, green and blue lines, respectively, which have PSF FWHM of ~ 6 nm) compared with the case where the source is located on the surface ($L - d = 0$). The question arises, why for the plasmonic
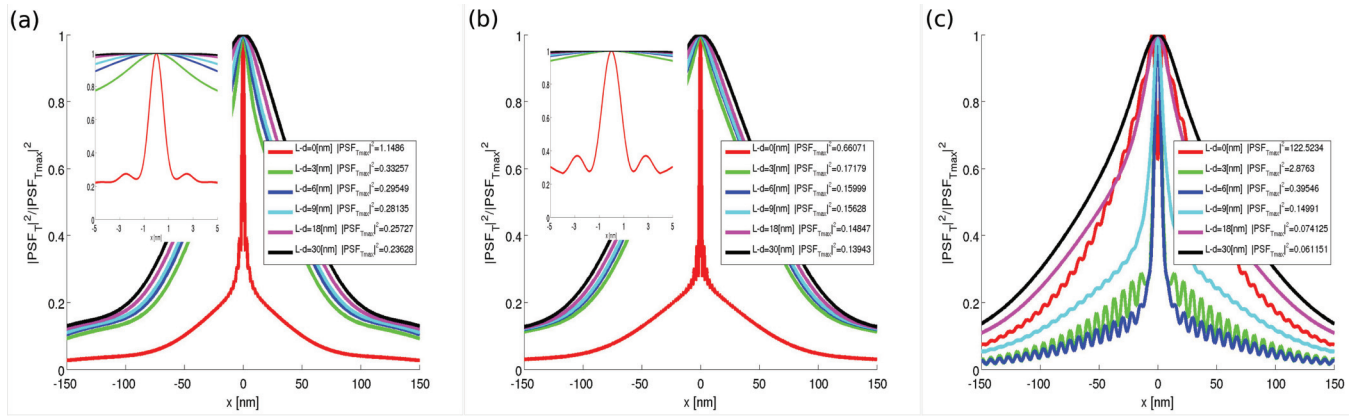
FIG. 3. (Color online) Normalized $PSF_T(x)$ calculated by Eq. (3), as a function of the transverse coordinate for several imaging distances, assuming slab thickness of $d = 3$ nm. The imaging distance $L - d$ and the normalization factor are shown in the legend. (a) $\omega = 1.31\omega_p$. (b) $\omega = 1.0681\omega_p$. The insets show a magnification of the PSF in the center. (c) $\omega = 0.7071\omega_p$.

resonance case, the PSF narrows with increasing imaging distance, while for the longitudinal mode case, the PSF always broadens with the increase in imaging distance. The underlying reason is revealed from the transmission spectrum, calculated for several imaging distances. In Figs. 4(a) and 4(b), we plot the transmission magnitude as a function of k_x of the $N = 11$

FP resonance at $\omega = 1.31\omega_p$ for $L - d = 0$ and $L - d = 6$ nm. It is seen that for k_x components larger than the vacuum light line (i.e., $k_x > 1.31\omega_p/c$), we obtain a rapid decay of the transmission for a distance of 6 nm, compared with the $L - d = 0$ case. This observation explains the broader PSF for the latter case [Fig. 3(a), blue versus red curve].
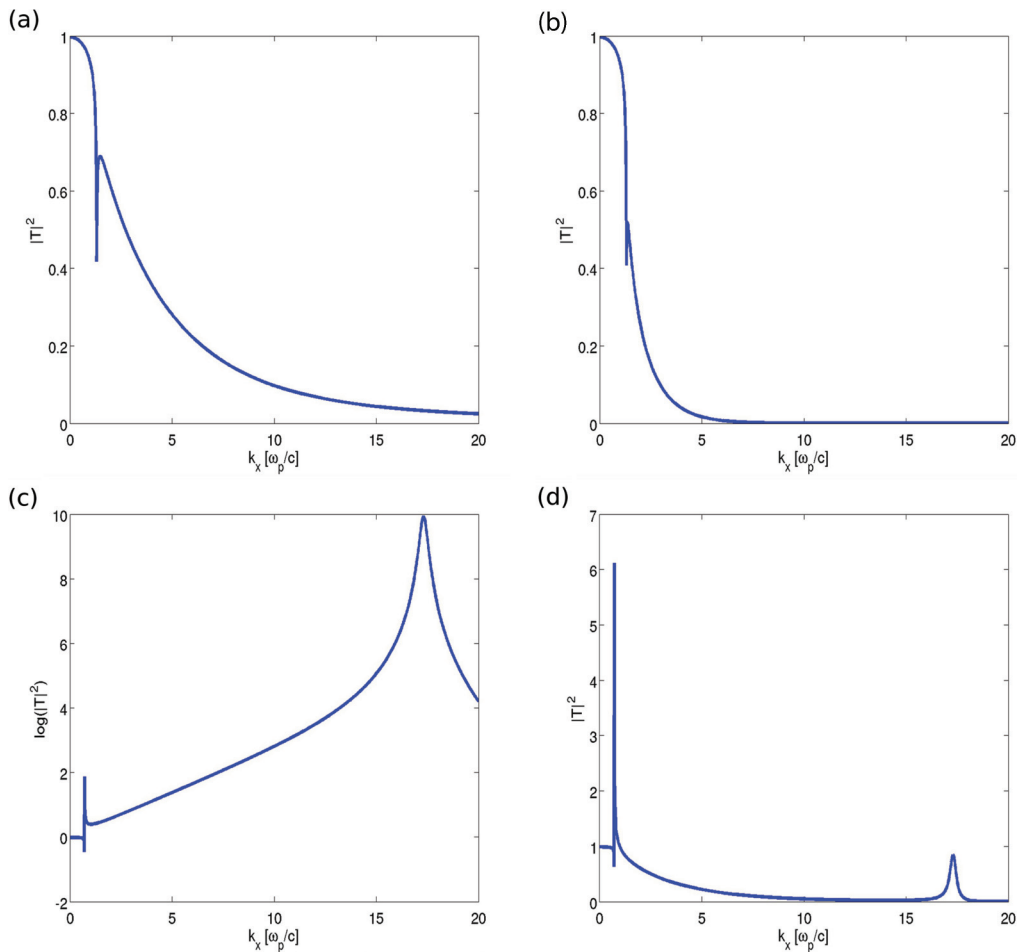

FIG. 4. (Color online) Transmission magnitude as a function of k_x. (a) $\omega = 1.31\omega_p$ and $L - d = 0$. (b) $\omega = 1.31\omega_p$ and $L - d = 6$ nm. (c) $\omega = 0.7071\omega_p$ and $L - d = 0$. (d) $\omega = 0.7071\omega_p$ and $L - d = 6$ nm.
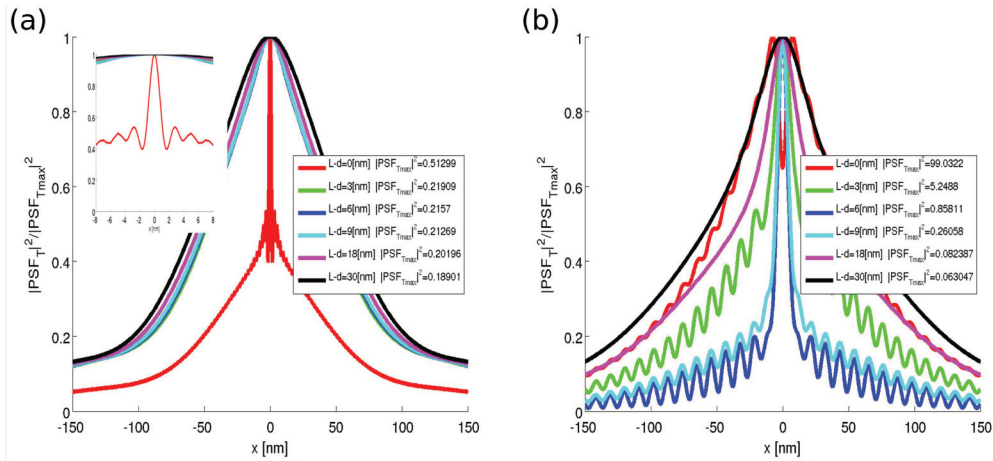
FIG. 5. (Color online) Normalized $PSF_T(x)$ calculated by Eq. (3), as a function of the transverse coordinate for several imaging distances. The imaging distance $L - d$ and the normalization factor are shown in the legend. The slab thickness is $d = 5$ nm. (a) $\omega = 1.217\omega_p$. The inset shows a magnification of the PSF in the center. (b) $\omega = 0.7071\omega_p$.

The transmission spectrum is also useful for explaining the PSF results of the plasmonic resonance. In Figs. 4(c) and 4(d), it is seen that for $L - d = 6$ nm the transmission spectrum is more flat as compared with the $L - d = 0$ case [mind that Fig. 4(c) is in logarithmic scale]. Therefore, the PSF becomes narrower [see Fig. 3(c), blue versus red line].

The relatively large imaginary component of $k_{z,L}$ sets a practical limitation on the slab thickness, preventing the use of slabs thicker than ∼10 nm. Indeed, this thickness is known to be the critical dimension for observing nonlocal effects in Ag [38]. By increasing d beyond 3 nm, the PSF becomes wider, and the transmission magnitude reduces. This is shown in Fig. 5 presenting the calculated PSF_T for $d = 5$ nm and two frequencies, $\omega = 1.217\omega_p$ (corresponding to the FP resonance with $N = 15$) and $\omega = 0.7071\omega_p$. The FWHM of PSF_T is now ∼6 nm for the longitudinal FP resonance case with $L - d = 0$, which is about three times larger than the FWHM obtained for $d = 3$ nm. For the plasmonic resonance case, the increase of the layer thickness has a more moderate effect. For the case shown in Fig. 3(c), with $L - d = 6$ nm, the FWHM is 8 nm, while for the case shown in Fig. 5(b) with $L - d = 6$ nm, the FWHM is found to increase only slightly, to ∼10 nm.

Finally, we consider the possibility of using a slab made of potassium (K) rather than Ag. We assume the following parameters for K [33]: $\omega_p = 3.72$ eV, $\gamma = (1/200)\omega_p$, and $v_F = 2.86 \times 10^{-3}c$. Because the plasma frequency of K is lower than that of Ag and is in the soft UV range, this metal might be more appealing for practical demonstrations of the SDL imaging effect in the UV, e.g., for lithography applications. In Figs. 6(a) and 6(b) we show the PSF for the $N = 3$ ($\omega = 1.062\omega_p$) and $N = 9$ ($\omega = 1.4915\omega_p$) FP resonances, calculated for a K layer thickness of $d = 3$ nm. In Fig. 6(c) we show the PSF for the plasmonic resonance case ($\omega = 0.7071\omega_p$). Because of the higher ohmic losses of this metal, the PSF in all three cases is evidently wider as compared to the Ag case. Yet, it may still be a more practical choice from the technological point of view [21].

IV. CONCLUSION

In conclusion, we have analyzed the scenario of SDL imaging based on longitudinal modes excited in a spatially dispersive metallic slab above the metal plasma frequency. Our results show that in this regime, for frequencies satisfying
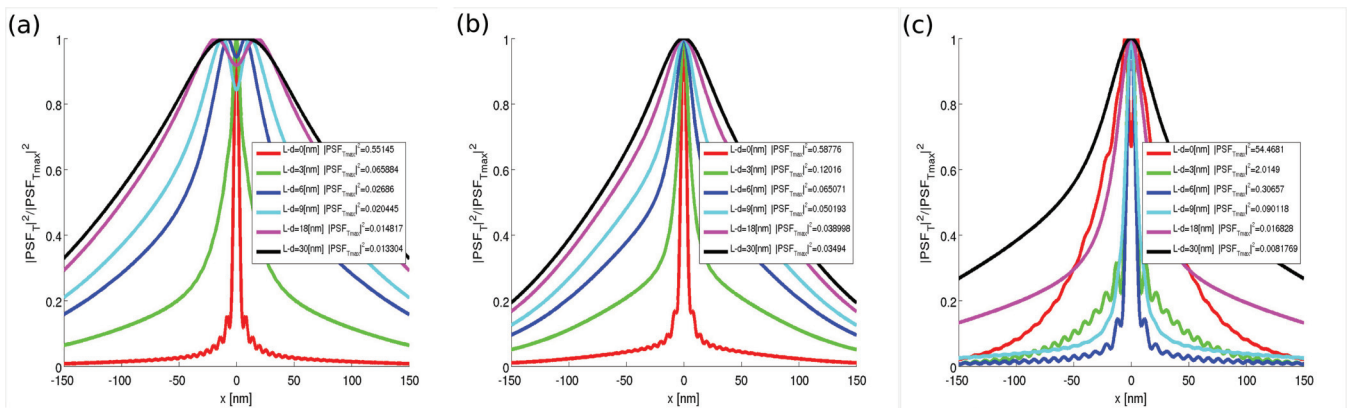

FIG. 6. (Color online) Normalized $PSF_T(x)$ calculated by Eq. (3), as a function of the transverse coordinate for several imaging distances, calculated for a potassium (K) layer with $d = 3$ nm. The imaging distance $L - d$ and the normalization factor are shown in the legend. (a) $\omega = 1.062\omega_p$ ($N = 3$). (b) $\omega = 1.4915\omega_p$ ($N = 9$). (c) $\omega = 0.7071\omega_p$ (plasmonic resonance).

$k_{z,L}d/\pi = N$ (N is an odd number) a transmission spectrum nearly flat with k_x is obtained, resulting in an ultranarrow PSF for the case of full contact ($L - d = 0$). This PSF is significantly more narrow than the one obtained with the conventional plasmonic based "poor man's lens" operated near $\omega_p/\sqrt{2}$. However, when $L - d$ is larger than a few nanometers, the situation is inverted and the plasmonic "poor man's lens" becomes a much better choice as it provides much narrower PSF. Another interesting difference is related to the wavelength of choice. With our proposed approach, the frequency of operation can be tuned (either by changing the layer thickness or by choosing a higher-order FP resonance), while for the SP resonance case the operation frequency is fixed in the vicinity of $\sim\omega_p/\sqrt{2}$. We believe that the proposed concept could have several useful applications for fields such as nanolithography, sensing, and microscopy, to name a few.

APPENDIX: CALCULATION OF THE TRANSMISSION AMPLITUDE FOR A SPATIALLY DISPERSIVE SLAB

For completeness, we derive here the expression for the transmission amplitude for the case of a spatially dispersive slab surrounded by local media. Similar derivations are available for the slab case [11,14,32] and the more general periodic case [38]. The slab geometry and the field amplitudes are depicted in Fig. 7. The incident and reflected amplitudes are denoted by E_0 and E_r, respectively. In the slab, we define two transverse mode amplitudes, E_1 and E_3, propagating and counterpropagating, respectively, and two longitudinal mode amplitudes, E_2 and E_4. The transmitted mode amplitude is E_t. To derive the complex transmission amplitude $T = E_t/E_0$,
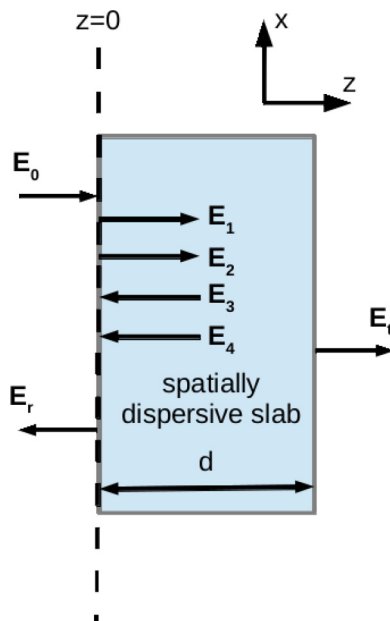

FIG. 7. (Color online) Schematic showing the field components of the various modes for the scenario of a spatially dispersive slab surrounded by local media.

we match all fields according to the assumed ABC. For this geometry, there are three types of incidence of the various modes:

(1) Transverse mode incident from a spatially nondispersive medium onto a spatially dispersive medium;

(2) Transverse mode incident from a spatially dispersive medium onto a spatially nondispersive medium;

(3) Longitudinal mode incident from a spatially dispersive medium onto a spatially nondispersive medium.

Employing the ABC, the transmission and reflection coefficients for these three incidence types can be derived:

$$R_{t1} = \frac{\varepsilon_T k_{z0} - k_{z,T} + (\varepsilon_T - 1)k_x^2/k_{z,L}}{\varepsilon_T k_{z0} + k_{z,T} - (\varepsilon_T - 1)k_x^2/k_{z,L}}, \quad \text{(A1a)}$$

$$T_{t1} = \frac{2k_{z0}}{\varepsilon_T k_{z0} + k_{z,T} - (\varepsilon_T - 1)k_x^2/k_{z,L}}, \quad \text{(A1b)}$$

$$T_{l1} = \frac{2k_{z0}(\varepsilon_T - 1)}{\varepsilon_T k_{z0} + k_{z,T} - (\varepsilon_T - 1)k_x^2/k_{z,L}}, \quad \text{(A1c)}$$

$$R_{l2} = \frac{2k_{z,T}(\varepsilon_T - 1)}{\varepsilon_T k_{z0} + k_{z,T} - (\varepsilon_T - 1)k_x^2/k_{z,L}}, \quad \text{(A1d)}$$

$$R_{t2} = \frac{k_{z,T} + (\varepsilon_T - 1)k_x^2/k_{z,L} - \varepsilon_T k_{z0}}{\varepsilon_T k_{z0} + k_{z,T} - (\varepsilon_T - 1)k_x^2/k_{z,L}}, \quad \text{(A1e)}$$

$$T_{t2} = \frac{2k_{z,T}\varepsilon_T}{\varepsilon_T k_{z0} + k_{z,T} - (\varepsilon_T - 1)k_x^2/k_{z,L}}, \quad \text{(A1f)}$$

$$R_{l3} = -\frac{k_{z,T} + (\varepsilon_T - 1)k_x^2/k_{z,L} + \varepsilon_T k_{z0}}{\varepsilon_T k_{z0} + k_{z,T} - (\varepsilon_T - 1)k_x^2/k_{z,L}}, \quad \text{(A1g)}$$

$$R_{t3} = -\frac{2k_x^2/k_{z,L}}{\varepsilon_T k_{z0} + k_{z,T} - (\varepsilon_T - 1)k_x^2/k_{z,L}}, \quad \text{(A1h)}$$

$$T_{t3} = -\frac{2\varepsilon_T k_x^2/k_{z,L}}{\varepsilon_T k_{z0} + k_{z,T} - (\varepsilon_T - 1)k_x^2/k_{z,L}}. \quad \text{(A1i)}$$

For these nine coefficients, R and T are for reflection and transmission, respectively. The subscripts l and t are for longitudinal and transverse modes, respectively, and the subscripts 1, 2, and 3 correspond to each of the three incidence types, respectively. For example, R_{t3} stands for the reflection coefficient of a transverse mode due to a longitudinal mode incident from a spatially dispersive medium onto air. We define six additional auxiliary transmission and reflection coefficients, based on those defined in Eqs. (A1): $\tilde{T}_{t2} = T_{t2}\exp(j\Phi_T)$, $\tilde{T}_{t3} = T_{t3}\exp(j\Phi_L)$, $\tilde{R}_{t2} = R_{t2}\exp(j2\Phi_T)$, $\tilde{R}_{t3} = R_{t3}\exp(j[\Phi_T + \Phi_L])$, $\tilde{R}_{l2} = R_{l2}\exp(j[\Phi_T + \Phi_L])$, and $\tilde{R}_{l3} = R_{l3}\exp(j2\Phi_L)$. Here, $\Phi_T = k_{z,T}d$ and $\Phi_L = k_{z,L}d$ are the phases accumulated by the transverse and longitudinal modes, respectively, when transversing the slab. With these definitions, we write a system of equation describing the mode amplitudes:

$$\begin{bmatrix} 0 & 0 & 0 & T_{t2} & T_{t3} & 0 & R_{t1} \\ 0 & 0 & 0 & R_{t2} & R_{t3} & 0 & T_{t1} \\ 0 & 0 & 0 & R_{l2} & R_{l3} & 0 & T_{l1} \\ 0 & \tilde{R}_{t2} & \tilde{R}_{t3} & 0 & 0 & 0 & 0 \\ 0 & \tilde{R}_{l2} & \tilde{R}_{l3} & 0 & 0 & 0 & 0 \\ 0 & \tilde{T}_{t2} & \tilde{T}_{t3} & 0 & 0 & 0 & 0 \\ 0 & 0 & 0 & 0 & 0 & 0 & 1 \end{bmatrix} \begin{bmatrix} E_r \\ E_1 \\ E_2 \\ E_3 \\ E_4 \\ E_t \\ E_0 \end{bmatrix} = \begin{bmatrix} E_r \\ E_1 \\ E_2 \\ E_3 \\ E_4 \\ E_t \\ E_0 \end{bmatrix}. \quad \text{(A2)}$$

The solution of the mode amplitudes are obtained by solving Eq. (A2):

$$E_1 = \left[\frac{T_{t1}\beta + T_{l1}\gamma}{\alpha\beta - \gamma\delta} \right] E_0, \tag{A3a}$$

$$E_2 = \left[\frac{T_{l1}\alpha + T_{t1}\delta}{\alpha\beta - \gamma\delta} \right] E_0, \tag{A3b}$$

$$E_3 = \tilde{R}_{t2} \left[\frac{T_{t1}\beta + T_{l1}\gamma}{\alpha\beta - \gamma\delta} \right] E_0 + \tilde{R}_{t3} \left[\frac{T_{l1}\alpha + T_{t1}\delta}{\alpha\beta - \gamma\delta} \right] E_0, \tag{A3c}$$

$$E_4 = \tilde{R}_{l2} \left[\frac{T_{t1}\beta + T_{l1}\gamma}{\alpha\beta - \gamma\delta} \right] E_0 + \tilde{R}_{l3} \left[\frac{T_{l1}\alpha + T_{t1}\delta}{\alpha\beta - \gamma\delta} \right] E_0, \tag{A3d}$$

$$E_t = \tilde{T}_{t2} \left[\frac{T_{t1}\beta + T_{l1}\gamma}{\alpha\beta - \gamma\delta} \right] E_0 + \tilde{T}_{t3} \left[\frac{T_{l1}\alpha + T_{t1}\delta}{\alpha\beta - \gamma\delta} \right] E_0, \tag{A3e}$$

$$E_t = \left[\frac{\tilde{T}_{t2}T_{t1}\beta + \tilde{T}_{t2}T_{l1}\gamma + \tilde{T}_{t3}T_{l1}\alpha + \tilde{T}_{t3}T_{t1}\delta}{\alpha\beta - \gamma\delta} \right] E_0. \tag{A3f}$$

Here we define $\alpha = (1 - R_{t2}\tilde{R}_{t2} - R_{t3}\tilde{R}_{l2})$, $\beta = (1 - R_{l2}\tilde{R}_{t3} - R_{l3}\tilde{R}_{l3})$, $\gamma = (R_{t2}\tilde{R}_{t3} + R_{t3}\tilde{R}_{l3})$, and $\delta = (R_{l2}\tilde{R}_{t2} + R_{l3}\tilde{R}_{l2})$. Equations (A3) describe all field amplitudes for this geometry.

[1] J. B. Pendry, Phys. Rev. Lett. **85**, 3966 (2000).
[2] V. G. Veselago, Sov. Phys. Usp. **10**, 509 (1968).
[3] R. E. Collin, J. PIER B **19**, 233 (2010).
[4] N. Fang, H. Lee, C. Sun, and X. Zhang, Science **308**, 534 (2005).
[5] D. Melville and R. Blaikie, Opt. Express **13**, 2127 (2005).
[6] W. Wu. Chaturvedi, V. J. Logeeswaran, Z. Yu, M. S. Islam, S. Y. Wang, R. S. Williams, and N. X. Fang, Appl. Phys. Lett. **96**, 043102 (2010).
[7] S. A. Ramakrishna, J. B. Pendry, D. Schurig, D. R. Smith, and S. Shultz, J. Mod. Opt. **50**, 1419 (2003).
[8] I. A. Larkin and M. I. Stockman, Nano Lett. **5**, 339 (2005).
[9] R. Ruppin, J. Phys. Condens. Matter **17**, 1803 (2005).
[10] R. Ruppin and K. Kempa, Phys. Rev. B **72**, 153105 (2005).
[11] C. David, N. A. Mortensen, and J. Christensen, Sci. Rep. **3**, 2526 (2013).
[12] V. M. Agranovich and V. L. Ginzburg, *Spatial Dispersion in Crystal Optics and the Theory of Excitons* (Springer-Verlag, Berlin, 1984).
[13] A. A. Rukhadze and V. P. Silin, Sov. Phys. Usp. **4**, 459 (1961).
[14] F. Forstmann and R. R. Gerhardts, *Metal Optics Near the Plasma Frequency* (Springer-Verlag, Berlin, 1986).
[15] A. D. Boardman and R. Ruppin, Surf. Sci. **112**, 153 (1981).
[16] P. J. Feibelman, Prog. Surf. Sci. **12**, 287 (1982).
[17] A. D. Boardman, *Electromagnetic Surface Modes* (Wiley, New York, 1982).
[18] J. M. Pitarke, V. M. Silkin, E. V. Chulkov, and P. M. Echenique, Rep. Prog. Phys. **70**, 1 (2007).
[19] G. W. Hanson, IEEE Antennas Propag. Mag. **52**, 198 (2010).
[20] N. A. Mortensen, S. Raza, M. Wubs, T. Søndergaard, and S. I. Bozhevolnyi, Nat. Comm. **5**, 3809 (2014).
[21] M. Anderegg, B. Feuerbacher, and B. Fitton, Phys. Rev. Lett. **27**, 1565 (1971).
[22] C. Ciracì, R. T. Hill, J. J. Mock, Y. Urzhumov, A. I. Fernández-Domínguez, S. A. Maier, J. B. Pendry, A. Chilkoti, and D. R. Smith, Science **337**, 1072 (2012).
[23] G. Toscano, S. Raza, A.-P. Jauho, N. A. Mortensen, and M. Wubs, Opt. Express **20**, 4176 (2012).
[24] S. Raza, N. Stenger, S. Kadkhodazadeh, S. V. Fischer, N. Kostesha, A.-P. Jauho, A. Burrows, M. Wubs, and N. A. Mortensen, Nanophotonics **2**, 131 (2013).
[25] P. Ginzburg and A. V. Zayats, ACS Nano **7**, 4334 (2013).
[26] T. V. Teperik, P. Nordlander, J. Aizpurua, and A. G. Borisov, Phys. Rev. Lett. **110**, 263901 (2013).
[27] R. Esteban, A. G. Borisov, P. Nordlander, and J. Aizpurua, Nature Comm. **3**, 825 (2012).
[28] L. Stella, P. Zhang, F. J. García-Vidal, A. Rubio, and P. García-González, J. Phys Chem. C **117**, 8941 (2013).
[29] R. C. Monreal, T. J. Antosiewicz, and P. Apell, New J. Phys. **15**, 083044 (2013).
[30] A. Moreau, C. Ciraci, and D. R. Smith, Phys. Rev. B **87**, 045401 (2013).
[31] M. Silveirinha, IEEE Trans. Antennas Propag. **54**, 1766 (2006).
[32] A. R. Melnyk and M. J. Harrison, Phys. Rev. B **2**, 835 (1970).
[33] M. G. Blaber, M. D. Arnold, and M. J. Ford, J. Phys. Chem. C **113**, 3041 (2009).
[34] W. H. Wee, and J. B. Pendry, Phys. Rev. Lett. **106**, 165503 (2011).
[35] B. Zhang and J. B. Khurgin, Appl. Phys. Lett. **98**, 263102 (2011).
[36] G. Rosenblatt, G. Bartal, and M. Orenstein, arXiv:1301.0105.
[37] W. C. Chew, *Waves and Fields in Inhomogeneous Media* (IEEE Press, Piscataway, NJ, 1995).
[38] A. Yanai, N. A. Mortensen, and U. Levy, Phys. Rev. B **88**, 205120 (2013).